Exploring Li-ion conductivity in cubic, tetragonal and mixed-phase Al-substituted $Li_7La_3Zr_2O_{12}$ using atomistic simulations and effective medium theory

Mauricio R. Bonilla,[*,†] Fabián A. García Daza,[†,‡] Javier Carrasco,[‡] and Elena Akhmatskaya[†,¶]

†*BCAM - Basque Center for Applied Mathematics, Alameda de Mazarredo 14, E-48009 Bilbao, Spain*

‡*CIC EnergiGUNE, Albert Einstein 48, E-01510 Miñano, Spain*

¶*IKERBASQUE, Basque Foundation for Science, María Díaz de Haro 3, E-48013 Bilbao, Spain*

E-mail: mrincon@bcamath.org

Abstract

Garnet $Li_7La_3Zr_2O_{12}$ (LLZO) is a promising solid electrolyte candidate for solid-state Li-ion batteries, but at room temperature it crystallizes in a poorly Li-ion conductive tetragonal phase. To this end, partial substitution of Li^+ by Al^{3+} ions is an effective way to stabilize the highly conductive cubic phase at room temperature. Yet, fundamental aspects regarding this aliovalent substitution remain poorly understood. In this work, we use molecular dynamics and advanced hybrid Monte Carlo methods for systematic study of the room temperature Li-ion diffusion in tetragonal and cubic LLZO to shed light on important open questions. We find that Al substitution

in tetrahedral sites of the tetragonal LLZO allows previously inaccessible sites to become available, which enhances Li-ion conductivity. In contrast, in the cubic phase Li-ion diffusion paths become blocked in the vicinity of Al ions, resulting in a decrease of Li-ion conductivity. Moreover, combining the conductivities of individual phases through an effective medium approximation allowed us to estimate the conductivities of cubic/tetragonal phase mixtures that are in good agreement with those reported in several experimental works. This suggests that phase coexistence (due to phase equilibrium or gradients in Al content within a sample) could have a significant impact on the conductivity of Al-substituted LLZO, particularly at low contents of Al^{3+}. Overall, by making a thorough comparison with reported experimental data, the theoretical study and simulations of this work advance our current understanding of Li-ion mobility in Al-substituted LLZO garnets and might guide future in-depth characterization experiments of this relevant energy storage material.

1. Introduction

Li-ion batteries (LIBs) are today's most effective commercial devices for electrochemical energy storage, offering superior volumetric and gravimetric energy density compared with other battery technologies.[1] However, LIBs typically contain highly flammable organic liquid electrolytes that limit their applicability in electric vehicles and stationary energy storage systems due to safety concerns.[1,2] This issue can be effectively mitigated by using solid electrolytes instead of liquid ones. Additionally, the high stability of solid electrolytes could enable metallic Li to replace graphite as negative electrode, potentially providing high energy density and long cycle life. As a consequence, all-solid-state LIBs are receiving increasing attention in battery research.[3–6]

$Li_7La_3Zr_2O_{12}$ (LLZO) garnet was initially synthesized and characterized by Murugan et al. in 2007,[7] and is regarded nowadays as a promising candidate electrolyte for all-solid-state LIBs. LLZO provides a high Li-ion conductivity, σ_{Li}, (between 10^{-3} and 10^{-4} S/cm at room

temperature),[7] outstanding chemical stability against high voltage positive electrodes and Li metal, thermal and mechanical robustness, and electrochemical inertness.[8] All this makes LLZO garnet an exceptionally well-suited solid electrolyte.[8,9]

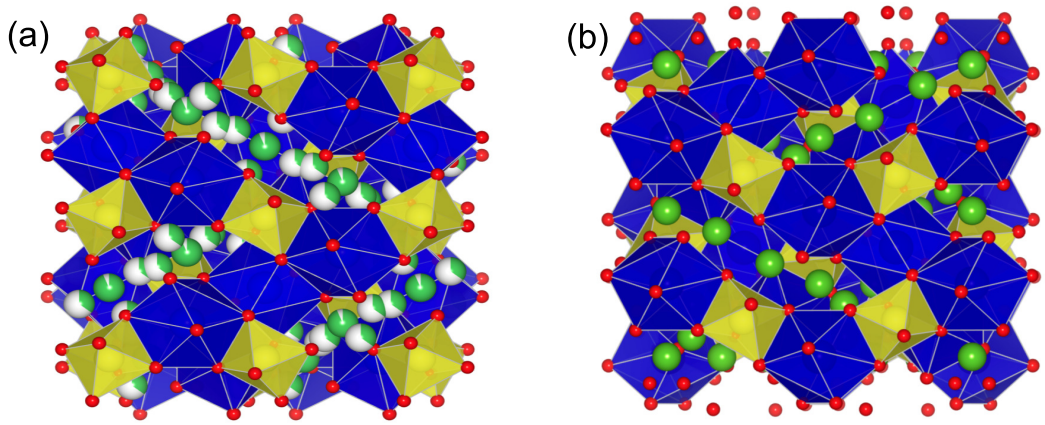

Figure 1: Crystal structures of garnet-type LLZO. (a) c-phase (SG Ia$\bar{3}$d). Li atoms are represented by partially filled spheres, indicating partial occupancy. (b) t-phase (SG I4$_1$/*acd*), containing an ordered distribution of fully occupied Li sites (Li ions are shown in green). La dodecahedra and Zr octahedra are shown in blue and yellow, respectively. The red spheres correspond to oxygen atoms.

LLZO garnets crystallize in a highly conductive cubic (c-) phase (Space Group Ia$\bar{3}$d), and a poorly conductive tetragonal (t-) phase (Space Group I4$_1$/*acd*).[10] t-LLZO is stable at room temperature and exhibits a completely ordered distribution of Li ions, while c-LLZO is only found at high temperatures ($>$ 400 K)[11,12] and contains a disordered sublattice of Li ions and Li vacancies. In the c-phase, Li ions are partially occupying 24d tetrahedral (Td) and 48g/96h octahedral (Oh) sites (see Fig. 1a). In contrast, three different Li sites are fully occupied in the t-phase, namely, 8*a* tetrahedral and two different distorted octahedral 16*f* and 32*g* sites (Fig. 1b). Substituting with supervalent cations increases the number of Li vacancies, and at sufficiently high cation concentrations the c-phase can be stabilized at room temperature. Most substitution strategies have been directed towards improving the Li-ion conductivity without blocking Li pathways, such as Te-,[13] Ta-[14–16] and Nb-substitution.[17] However, substitution in LLZO can also involve the Li sublattice itself, directly obstructing the diffusion path of Li ions. In particular, the substitution of Li^+ by Ga^{3+}[18–22] and Al^{3+}[23–41]

ions has been extensively investigated in the last years.

Substituting LLZO with Ga ions yields relatively consistent experimental ionic conductivities around $\sim 10^{-3}$ S/cm, slightly decreasing with increasing Ga content.[20–22] In contrast, there is significant variability in the literature regarding the conductivity of $Li_{7-3x}Al_xLa_3Zr_2O_{12}$ (Al_x-LLZO), with σ_{Li} spanning between $\sim 10^{-6}$ and $\sim 10^{-3}$ S/cm for x in the range 0 - 0.25 per formula unit (pfu).[10,38] Moreover, there seems to be no precise trend in the variation of σ_{Li} with x. For example, impedance spectroscopy measurements from Cheng et al.[27] displayed an increase or a decrease in σ_{Li} with x depending on the calcining regime of the sample. Wachter-Welzl et al.,[41] on the other hand, obtained variations of up to 2 orders of magnitude for 44 samples of $Al_{0.2}$-LLZO, sintered at temperatures of 1150 and 1230 °C. These authors also reported an inhomogeneous behaviour of σ_{Li} when varying the size of the samples, possibly caused by a non-uniform distribution of Al atoms within the garnet. In addition, there is no experimental consensus on the exact Al content that triggers the tetragonal-to-cubic phase transition in Al_x-LLZO. Matsuda et al.[30] determined that their samples contained only t-phase for $x < 0.20$, whereas other authors have reported only c-phase[40] or a combination of c- and t-phases[33–35,42] for x between 0.1 and 0.20. Clearly, this can have a great impact on discerning the σ_{Li} variation as a function of x in Al_x-LLZO.

Figure 2 summarizes the observed variability of σ_{Li} in the literature. Understanding the origin of such large variability is important because the search for optimal designs of Al_x-LLZO is an active area of research.[6] Yet, the observed high sensitivity of measured σ_{Li} towards experimental and processing conditions hinders progress in this direction. Therefore, it is relevant to determine from a theoretical standpoint what the maximum attainable σ_{Li} is, and how it varies with Al content in a perfectly non-porous, 100% pure Al_x-LLZO garnet. This information can guide synthesis efforts to focus on the most promising Al concentrations and ultimately optimize σ_{Li}.

Whilst force-field simulation studies have largely focused on the diffusion of Li ions in pristine LLZO,[43–46] Ta-[46] and Ga-substituted LLZO,[22] to the best of our knowledge, no reports

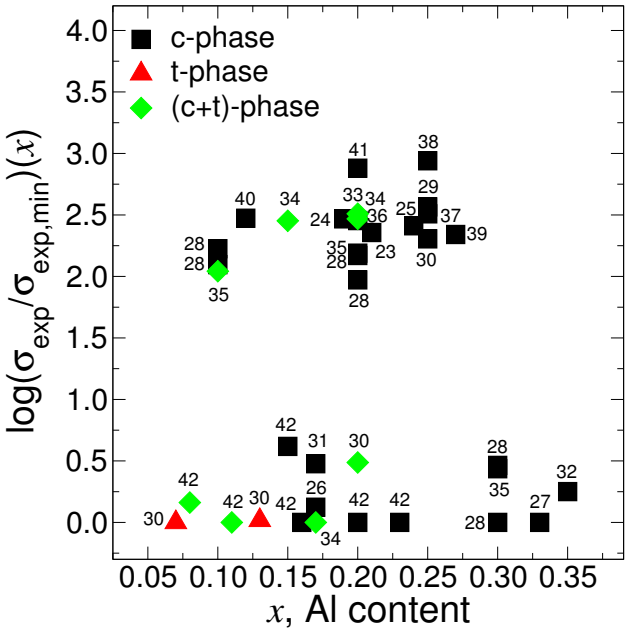

Figure 2: Experimental ionic conductivity ratio $\log(\sigma_{\text{exp}}/\sigma_{\text{exp, min}})$ as a function of Al content, x, at 298 K in Al_x-LLZO. σ_{min} refers to the lowest conductivity at each concentration. The square, triangle and diamond symbols correspond to experimental data in cubic, tetragonal and a combination of both phases, respectively. Data are taken from individual experimental works, and the numbers next to each data point correspond to the reference numbers for each source.

have been published on force-field simulations of ionic transport in Al-substituted LLZO. Nonetheless, density functional theory (DFT) calculations have provided valuable insights into the local environment around Al ions,[36,47] suggesting that the presence of Al in the Td sites leads to a slight reduction of the energy gap between the neighboring O_h and Td sites, which favors Li-ion hopping. However, long range, collective mechanisms affecting diffusion are not readily accessible with small supercell DFT calculations due to computational limitations. This is precisely the domain in which force-field simulations are most useful, provided the proposed interaction potentials are sufficiently accurate and configurational sampling is efficient. In this work, we use molecular dynamics (MD) and the advanced atomistic simulation technique, Generalized Shadow Hybrid Monte Carlo Method (GSHMC),[48] to study ionic diffusion at room temperature in Al_x-LLZO in both t- and c-phases. We focus on the room temperature because of its practical relevance and abundance of experimental data. Under some circumstances, GSHMC allows for more efficient sampling than traditional MD, reducing the computational effort required to determine thermodynamic and dynamical properties of slowly diffusing ions in solid state systems,[49,50] such as the one at hand.

In this study, we provide ideal upper and lower limits for σ_{Li} in Al_x-LLZO, and demonstrate that in a perfect c-phase garnet the addition of Al leads to a monotonic reduction of σ_{Li}. In contrast, σ_{Li} increases in t-Al_x-LLZO when increasing the Al content. This phenomenon is explained by examining the integrated radial distribution functions. The possibility of c- and t- phase coexistence has been proposed by several authors and it could partially explain why the deviations between simulated and experimental data are particularly large at low values of x. So, in addition, we use effective medium theory to examine the proportions under which c- and t-phases would need to coexist in order to reproduce reported experimental conductivities.

The paper is structured as follows: In Section 2, the details of the atomistic models and the corresponding force-field parameters specifically derived for c- and t-Al_x-LLZO are provided. In section 3, the diffusion of Li ions through both phases at room temperature is

estimated using MD and GSHMC simulations (Subsection 3.1). Afterwards, our predictions are compared with the available experimental data, including Li-ion conductivities in c-phase, t-phase and a combination of both phases at several Al contents (Subsection 3.2). Lastly, the effects of Al substitution and phase coexistence on long range Li-ion mobility are summarized in Section 4.

2. Computational Methodology

2.1 Force-field parameterization

The potential energy between atoms in Al_x-LLZO was calculated using the Coulomb-Buckingham interatomic potential U_{ij}:

$$U_{ij} = \frac{q_i q_j}{4\pi\epsilon|\mathbf{r}_{ij}|} + A_{ij}\exp\left(-B_{ij}\,|\mathbf{r}_{ij}|\right) - \frac{C_{ij}}{|\mathbf{r}_{ij}|^6}, \tag{1}$$

where, ϵ is the vacuum permittivity, $|\mathbf{r}_{ij}|$ is the distance between atoms i and j, q_i and q_j are their respective charges and $A_{ij} \geq 0$, $B_{ij} > 0$ and $C_{ij} \geq 0$ are the parameters of the Buckingham potential. In this work, force-field parameters for LLZO garnet in c- and t-phases were taken from the works of Jalem et al.[22] and Klenk and Lai,[51] respectively, whereas the parameters from Pedone et al.[52] were considered for interactions with Al ions.

In order to optimize the force-field parameters for the simulation of Al_x-LLZO, we fine-tuned the Li-O interaction in the case of the c-phase, whilst for the t-phase, both Li-O and Al-O interactions were fitted until the predicted cell dimensions were within 0.1% of the experimental value for each concentration x. For the c-phase, we selected $x = [0.10, 0.12, 0.15, 0.17, 0.20, 0.25]$ due to the availability of experimental data. For the t-phase we chose $x = [0.10, 0.12, 0.15, 0.17, 0.20]$ either because experimental data was available or to compare with the corresponding diffusivity in the c-phase. The precise protocol is described in the following.

2.1.1 *Selection of configurations with minimal electrostatic energy for each x in* Al_x-LLZO*:* We considered $3 \times 3 \times 3$ Al_x-LLZO supercells, containing 1944 available Li-ion sites, 648 La atoms, 432 Zr atoms, and 2592 O atoms. Al cations were inserted into randomly selected Li-ion sites, which generated two Li vacancies per inserted Al ion as a result of electroneutrality preservation. Consequently, a large number of possible configurations for distributing the Li ions, Li vacancies and Al ions within the Li sublattice became available. In order to make an adequate selection of low-energy structures, we chose to sample the electrostatic energy only (using the formal charges of the ions) of 10000 randomly generated configurations for each x because most of the contribution to the total potential energy is expected to be electrostatic (Figure 3).

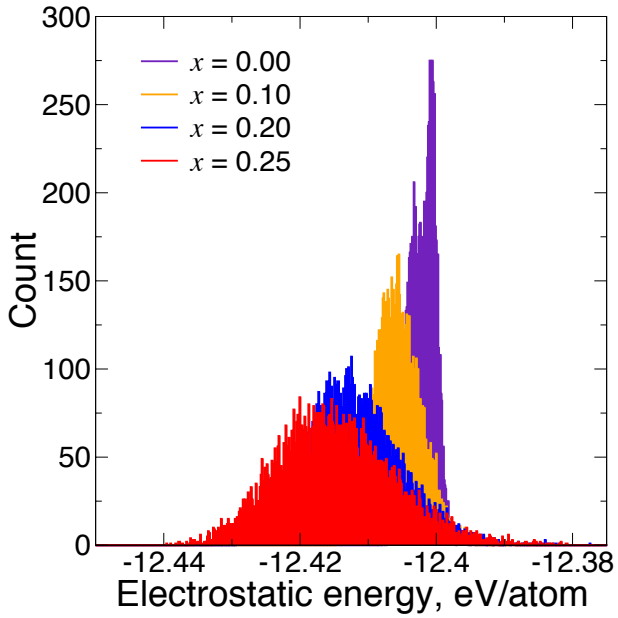

Figure 3: Computed electrostatic energy distributions resulting from 10000 Li/vacancy/Al randomly generated configurations in c-Al_x-LLZO.

Figure 3 depicts the resulting electrostatic energy distributions for $x = 0.0, 0.10, 0.20$, and 0.25 in the c-Al_x-LLZO. According to Fig. 3, increasing the amount of Al ions displaces the mean energy towards more negative values. This is because the increase of Li vacancies increases the average distance between Li-Li and Li-Al ions, leading to the decrease of the total

electrostatic repulsion. However, increasing x also widens the distribution considerably, because a larger number of configurations involve Al ions close enough to experience significant Coulombic repulsion. Similar tendencies are reported by Jalem et al.[22] and García et al.[53] for Ga substituted LLZO. The analogous trend was observed in the histograms corresponding to t-Al$_x$-LLZO (not shown). It is interesting to note that for $x = 0.10$ over 98% of the generated configurations did not differ from each other by more than 20 meV/atom, whereas for $x = 0.25$ this number increased to 60 meV/atom. Thus, it is likely that for $x > 0.10$, a careful selection of appropriate structures for conductivity analysis is of paramount importance. On the contrary, for $x < 0.10$, nearly all configurations are energetically equivalent. Following previous studies,[22,54–56] we selected the structures with the lowest energy for each x for the force-field optimization and molecular simulations in the following secions.

2.1.2 *Optimization of the force-field parameters*: We selected the unit cell parameters reported in references 26, 34, 35, 38, 40 and 57 at $x = 0.10,\ 0.12,\ 0.15,\ 0.17,\ 0.20$ and 0.25, respectively, as representative target values to adjust the force-field parameters $B_{\text{Li-O}}$ for the c-phase. For the t-phase, the structural parameters reported by Djenadic et al.[42] and Botros et al.[34] were considered as target values to fit $B_{\text{Li-O}}$, $A_{\text{Al-O}}$ and $B_{\text{Al-O}}$. Since there are only one target structural parameter and one parameter to optimize in the c-phase force-field, the procedure was done simply by repeatedly performing 1 ns long NPT MD simulations and adjusting $B_{\text{Li-O}}$ manually until satisfactory agreement was achieved. For the t-phase the optimization was more complex, given that there are two structural parameters to target and three force-field parameters to fit. Therefore, the parameters were adjusted using the nonlinear conjugate gradient method as implemented in the SciPy library of Python. The final set of force-field parameters are listed in Tables 1 and 2.

2.2 Simulation Setup

Atomistic simulations were performed with the MultiHMC-GROMACS software package,[58,59] an in-house modified version of the open-source package GROMACS 4.5.4.[60] MultiHMC-

Table 1: Buckingham parameters for c-Al_x-LLZO. Table (a) shows the nominal values reported by Jalem et al.[22] Modified values of parameter $B_{\text{Li-O}}$ as a function of the Al content are listed in Table (b). The interaction parameters between Al and O atoms are taken from Ref. 52.

(a)

$i-j$ pair	A_{ij} (eV)	B_{ij} (Å^{-1})	C_{ij} (eV Å^6)
$Al^{2.1+}$ - $O^{1.4-}$	7042.59	4.316	101.50
$Li^{0.7+}$ - $O^{1.4-}$	876.86	4.110	0.00
$La^{2.1+}$- $O^{1.4-}$	14509.63	4.102	30.83
$Zr^{2.8+}$- $O^{1.4-}$	2153.80	3.439	0.00
$O^{1.4-}$ - $O^{1.4-}$	4869.99	4.163	27.22

(b)

x	$B_{\text{Li-O}}$ (Å^{-1})
0.10	3.892
0.12	3.892
0.15	3.892
0.17	3.880
0.20	3.861
0.25	3.863

Table 2: Buckingham parameters for t-Al_x-LLZO. Table (a) shows the nominal values reported by Klenk and Lai.[51] Modified values of parameters $B_{\text{Li-O}}$, $A_{\text{Al-O}}$, $B_{\text{Al-O}}$ and $C_{\text{Al-O}}$ as a function of Al content are listed in Table (b). Interaction parameters between Al and O atoms are taken from Ref. 52.

(a)

$i-j$ pair	A_{ij} (eV)	B_{ij} (Å^{-1})	C_{ij} (eV Å^6)
$Al^{3.00+}$ - $O^{1.65-}$	7042.59	4.316	101.50
$Li^{1.00+}$ - $O^{1.65-}$	1087.29	3.846	0.00
$La^{2.50+}$- $O^{1.65-}$	2075.26	3.068	23.25
$Zr^{2.65+}$- $O^{1.65-}$	1650.32	3.215	5.10
$O^{1.65-}$ - $O^{1.65-}$	4870.00	3.745	77.00

(b)

x	$B_{\text{Li-O}}$ (Å^{-1})	$A_{\text{Al-O}}$ (eV)	$B_{\text{Al-O}}$ (Å^{-1})	$C_{\text{Al-O}}$ (eV Å^6)
0.10	6.667	35356.00	3.510	0.00
0.12	5.000	35356.00	3.510	0.00
0.15	3.846	35356.00	4.257	0.00
0.17	3.846	35356.00	4.257	0.00
0.20	3.846	35356.00	4.257	0.00

GROMACS supports all algorithms implemented in GROMACS and, apart from this, offers access to various hybrid Monte Carlo (HMC) methods[48,61] and multi-stage integrators[59,62] recently developed for molecular simulations.

In addition to conventional molecular dynamics (MD) simulations, we also used the generalized hydrid Monte Carlo (GSHMC) method by Akhmatskaya and Reich.[48] The GSHMC is an importance sampling generalized hybrid Monte Carlo (GHMC)[63,64] where sampling is performed with respect to modified Hamiltonians. Compared to HMC, GSHMC achieves higher acceptance rates and preserves dynamical information, whereas its advantages over MD are in its ability to rigorously maintain a simulation temperature and sample broadly. The GSHMC method has been successfully employed in the study of rare events in biological systems,[58,65–67] and ion mobility in solid battery materials.[49,50,53] A theoretical description of the GSHMC method and details of its implementation have been published elsewhere.[48,58,62,67]

To compare sampling efficiency of MD and GSHMC methods, we measured the integrated autocorrelation functions ($IACF$) of potential energy U

$$IACF^U = \sum_{l=0}^{K'} ACF(l), \tag{2}$$

where $ACF(l), l = 0, \ldots, K \leq K'$ is the standard autocorrelation function for the time series U_k of K samples, $k = 1, \ldots, K$. Lower values of $IACF$ indicate a more efficient sampling since it estimates the time required, on average, to generate an uncorrelated sample. In Fig. 4, we present the values of $IACF^U_{\mathrm{MD}}/IACF^U_{\mathrm{GSHMC}}$ for $Al_{0.10}$-LLZO and $Al_{0.12}$-LLZO in t-phase and $Al_{0.20}$-LLZO and $Al_{0.25}$-LLZO in c-phase at room temperature during the equilibration stage in the NVT ensemble. GSHMC sumulations exhibit a sampling performance up to 25 times better than MD for the tested systems in the t-phase. In contrast, for the c-phase the performances of both methods are comparable. Based on this analysis, GSHMC simulations of Al_x-LLZO have only been performed for the t-phase (x =0.10, 0.12, 0.15, 0.17 and 0.20)

in order to take advantage of its enhanced sampling performance. For the simulation of c-Al$_x$-LLZO (x =0.10, 0.12, 0.15, 0.17, 0.20 and 0.25) we chose to use the conventional MD approach in order to minimize the efforts required for tunning the simulation parameters in GSHMC.

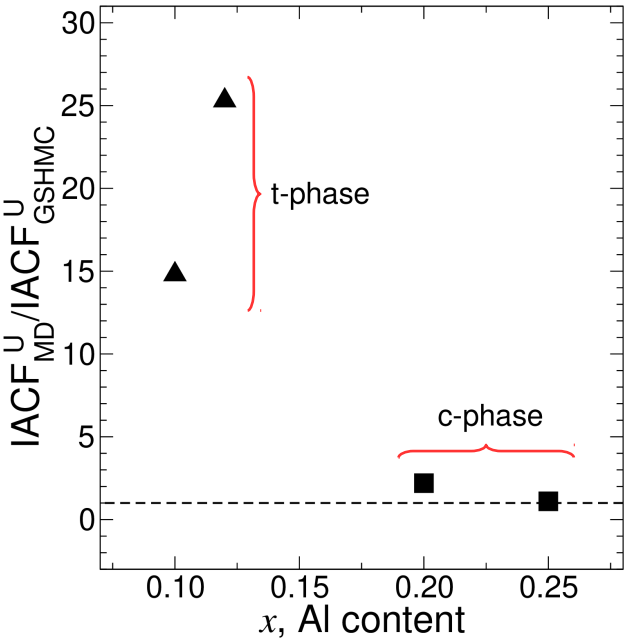

Figure 4: Relative $IACF^U$ with respect to GSHMC at T = 298 K achieved when calculating the potential energy during the equilibration stage with the MD method.

Tunnable input parameters in GSHMC include the MD trajectories length (L), time step (Δt), partial velocity update parameter (ϕ), and the order of a modified Hamiltonian. In contrast, only the time step (Δt) has to be defined for MD simulations. We determined the GSHMC parameters following our previous work on Al/Ga co-substituted LLZO systems.[53] The validated GSHMC parameters resulted in L = 150, Δt = 4.0 fs, ϕ = 0.3 and the 4$^{\text{th}}$ order modified Hamiltonian for GSHMC. We combined GSHMC with the two-stage M-BCSS integrator specifically derived for GSHMC,[68] which allowed us to use the time step as long as 4.0 fs. In MD simulations, the Verlet integrator has been applied with the time step of 2 fs. Production runs of 30 ns and 120 ns were needed to observe the main transport features in the case of c- and t-phases, respectively.

3. Results and Discussion

3.1 Diffusion

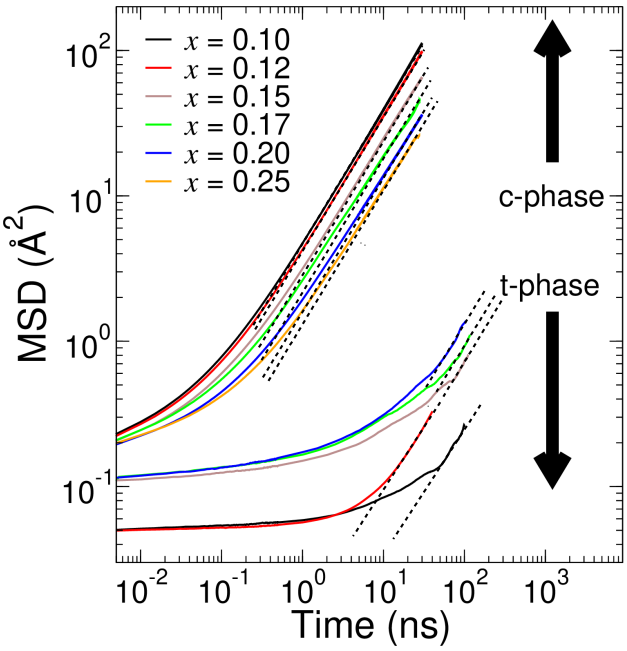

Figure 5: Mean-squared displacement of Li ions as a function of x in Al$_x$-LLZO garnet at room temperature. The dashed lines have a slope of unity and represent the diffusional regime.

Figure 5 depicts the mean-squared displacement (MSD) of Li ions for c- and t-Al$_x$-LLZO at room temperature. Clearly, the simulation time required to adequately capture the diffusional regime, t_0 (slope of unity on the log-log plot), is significantly higher for the t-phase than for the c-phase. To better appreciate this difference, the values of t_0 are reported in Table 3. Our simulations show that t_0 in c-Al$_x$-LLZO is between one and two orders lower than in t-Al$_x$-LLZO. This result reflects the differences between the energy barriers for a Li-ion jump in the t-phase (0.4 - 0.6 eV)[69,70] and the c-phase (0.1 - 0.3 eV).[45,71] Indeed, with $k_BT = 0.025$ eV at $T = 298$ K, and a difference of ~ 0.1 eV between the energy barriers, the ratio of the diffusivities in the c- and t-phases is expected to be between one and two orders of magnitude.

Table 3: Diffusion coefficient D_{Li}, onset time of diffusion t_0 as a function of Al content (x) in c- and t-Al$_x$-LLZO. For c-Al$_x$-LLZO, the parameter d (see eq. 5) and the rate of decrease of d with x are also provided.

Phase	x	D_{Li} (cm^2/s)	t_0 (ns)	d (Å)	dd/dx (Å)
c	0.10	5.5×10^{-8}	0.63	1.44	–
c	0.12	5.1×10^{-8}	0.65	1.42	-0.9
c	0.15	3.3×10^{-8}	0.70	1.17	-8.3
c	0.17	2.2×10^{-8}	0.78	1.01	-8.0
c	0.20	1.7×10^{-8}	1.00	1.00	-0.3
c	0.25	1.3×10^{-8}	1.20	0.98	-0.4
t	0.10	2.3×10^{-11}	40.0	–	–
t	0.12	5.8×10^{-11}	25.0	–	–
t	0.15	5.8×10^{-11}	52.0	–	–
t	0.17	2.1×10^{-10}	41.0	–	–
t	0.20	2.1×10^{-10}	40.0	–	–

Additionally, we computed the diffusion coefficient of Li ions, D_{Li}, as

$$D_{\mathrm{Li}} = \lim_{t\to\infty} \frac{1}{6t} \langle |\mathbf{r}_i(t) - \mathbf{r}_i(0)|^2 \rangle_i, \tag{3}$$

where $\mathbf{r}_i(t)$ is the position of Li ion i at time t. The corresponding values of D_{Li} at each x are also given in Table 3. For c-Al$_x$-LLZO we see a monotonic decrease of D_{Li} with x, indicating that the addition of Al to c-LLZO is detrimental to Li-ion mobility. Interestingly, t_0 increases monotonically with x, which suggests that the decrease of D_{Li} with x can be partially explained by an increase in the average residence time of Li ion in the Li sites. In contrast, D_{Li} increases monotonically with x for t-LLZO, while t_0 does not display any specific trend. This behaviour is certainly intriguing and will be tackled in detail below.

In the previous work,[53] the decrease of ionic conductivity with Al content in c-LLZO was explained in terms of the distribution of Li ions and Li-vacancies around tetrahedral Al ions. By analyzing the Al-Li pair correlations with respect to three families of Li ions: static (do not displace to adjacent sites throughout the entire simulation run), diffusing short-range

(displacement occurs within nearest neighbors only) and diffusing long-range (displacement occurs beyond nearest neighbors) we found that Al ions "trap" their associated Li vacancies in order to reduce the local electrostatic energy. More surprisingly, Li ions up to the second nearest neighbors from an Al ion (~ 5Å) are not available for long range diffusion. Hence, as the Al content increases and clusters start to form, a significant volume fraction of the crystal begins to harbor Li ions that are unable to diffuse, negatively impacting the conductivity. Here, we also analyze the radial distribution functions to explain the diffusivity increase with Al content in substituted t-LLZO. Fig. 6 shows the average number of Li ions $\langle n_{\mathrm{Li}}(r)\rangle$ allocated within a distance r from a tetrahedrally coordinated Li ion, $\mathrm{Li_{Td}}$ (solid line), and a tetrahedrally coordinated Al ion, $\mathrm{Al_{Td}}$ (dashed line), in both (a) t-LLZO and (b) c-LLZO. The curves were computed as

$$\langle n_{\mathrm{Li}}(r)\rangle = 4\pi \int_0^r g_{\mathrm{X_{Td-Li}}}(r) r^2 dr, \tag{4}$$

where $g_{\mathrm{X_{Td-Li}}}$ is the radial distribution function between $\mathrm{Al_{Td}}$(or $\mathrm{Li_{Td}}$) and the surrounding Li ions. In Fig. 6 we only show $g_{\mathrm{Al_{Td-Li}}}$ obtained from the simulations of the $\mathrm{Al_{0.2}}$-LLZO system; however, the results are consistent accross all of the investigated Al contents.

For c-LLZO (Fig. 6(b)), the dashed line always remains under the solid line, indicating that, in average, there are less Li ions surrounding an $\mathrm{Al_{Td}}$ than a $\mathrm{Li_{Td}}$. In contrast, for t-LLZO (Fig. 6(a)) the dashed line is above the solid line for $3.8 < r < 4.5$ Å. Analysis of the simulation snapshots revealed a striking feature in t-LLZO, schematically described in polyhedral ring topologies in the insets of Fig. 6(a): In pristine t-LLZO (top inset), Li ions are ordered over two tetrahedra and six octahedra in each ring; four Td sites are not accessible to Li (in gray). Insertion of Al in an accessible Td site leads to strong electrostatic repulsion with the neighboring octahedral Li ions, pushing some of them to partially occupy previously inaccessible Td sites (now distorted). Adding these tetrahedra to the set of available sites improves network connectivity, as it likely reduces the energy required to access the Oh sites coordinating the distorted Td sites.

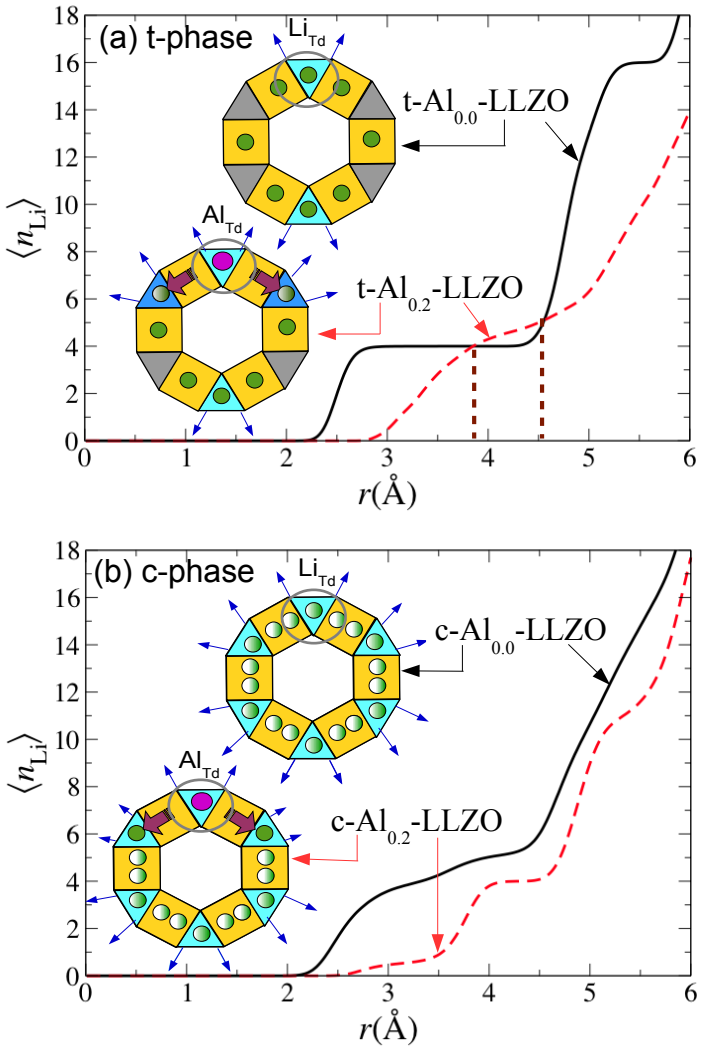

Figure 6: Local impact of Al substitution in t-LLZO and c-LLZO. The solid line represents the average number of Li ions, $\langle n_{\mathrm{Li}}(r)\rangle$, allocated within a distance r from a tetrahedral Li-ion ($\mathrm{Li_{Td}}$) in pristine (a) t-phase and (b) c-phase LLZO. The dashed line represents the value of $\langle n_{\mathrm{Li}}(r)\rangle$ within a distance r from a tetrahedral Al ion ($\mathrm{Al_{Td}}$) in (a) t-phase $\mathrm{Al}_{0.2}$-LLZO and (b) c-phase $\mathrm{Al}_{0.2}$-LLZO. Schematics of the pristine and substituted polyhedral ring topologies are shown as insets: the triangles are Td sites and the rectangles Oh sites, while the green circles correspond to Li ions (partial filling denotes partial occupancy) and the purple one to an Al ion. The blue arrows indicate active diffusion paths from Td sites. In pristine t-LLZO, many available Td sites are not accessible (in gray), whereas in pristine c-LLZO the Li ions are disordered over all available sites.

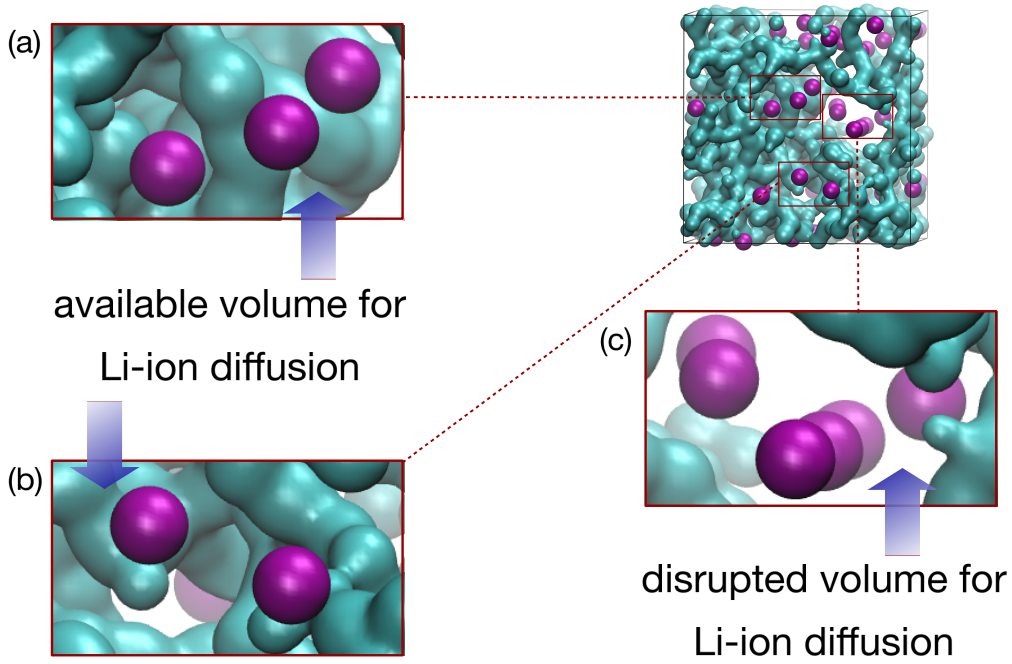

Figure 7: MD snapshot depicting an effect of Al substitution on the volume density of diffusing Li ions (shown in green) for c-LLZO. Here, diffusing Li ions are defined as those displacing over 4 Å during the course of a simulation run. Al ions are represented by magenta spheres. There are no diffusion paths within 4-5 Å of a tetrahedrally coordinated Al. (a) Three neighboring Al ions (8 Å from each other) generate a significant disruption on the volume available for Li diffusion. Similarly, the presence of only two Al ions (b) do not considerably decrease the disrupted volume. Moreover, increasing of substituent cations (c) decrease the presence of active diffusion channels by suppressing volume density regions near the Al ions.

In pristine c-LLZO (6(b)) the Li ions are disordered over all available sites (top inset). The addition of Li vacancies as the Al content increases does not reduce the average residence time of Li in the lattice sites of the c-phase, because Al cations are likely to permanently 'capture' most of their associated vacancies, rendering them futile in enhancing Li mobility. Moreover, our recent work[53] indicates that Li ions in the nearest Td sites from an Al_{Td} are essentially static, increasing the occupancy to nearly unity (see bottom inset of Fig. 6(b)).

Let us examine more closely the relationship between t_0 and D_{Li} in c-LLZO. Given that Li-ion diffusion occurs as a series of jumps between adjacent crystallographic sites, t_0 is roughly equivalent to the average residence time of a Li ion in a Li site and inversely proportional to D_{Li}.[72,73] Under ideal conditions, the proportionality constant corresponds to the ratio between the inter-site distance and the coordination number, but the complex geometry of the Li sublattice (containing two different sites O_{h} and T_{d}) and correlations between neighboring Li ions generate deviations from this interpretation. Nevertheless, some interesting insights can be obtained by estimating the proportionality constant through

$$D_{\mathrm{Li}}^{eff} = d^2/(6t_0), \tag{5}$$

where d represents an effective distance between neighboring sites in a uniform lattice with the same average residence time t_0 at each Al content. It should be stressed that d does not represent the actual inter-site distance, but a measure of the average distance a Li ion displaces divided by the number of jumps. In order to extract d, we equate D_{Li}^{eff} (eq. 5) and D_{Li} (eq. 3). The resulting values are reported in Table 3. Interestingly, d decreases monotonically with increasing x, suggesting that the increasing value of t_0 does not entirely explain the variation of D_{Li} with x in the c-phase. If that was the case, d would be expected to vary in a non systematic way around an average value. Moreover, the rate of decrease in d is not uniform: indeed, d decreases sharply between $x = 0.12$ and 0.17, and continues to decrease at a slower rate between $x = 0.17$ and to 0.25 (see $\mathrm{d}d/\mathrm{d}x$ in Table 3). The initially fast reduction in d is related to the fact that pairs and triplets of neighboring Al cations

begin to appear as x increases, reducing the availability of volume through which diffusion can occur and, therefore, hindering actual long range Li-ion displacement. In other words, at low values of x the formation of small Al-ion cluster (groups of Al ions separated by less than 10 Å) turns some regions of the structure inaccessible to Li ions. This pushes some Li-ion to the vicinity of their initial position upon several jumps. As the Al content increases beyond $x = 0.12$, additional Al ions may end up belonging to already existing Al-ion cluster through which diffusion was already not possible. This obviously results in a slower reduction of the volume available for diffusion. Such situations are illustrated in Fig. 7. The formation of these clusters is detailed in a previous paper,[53] but the variation of their size and impact on D_{Li}^{eff} with x has not been described before.

3.2 Conductivity

Figure 8 presents the experimental and simulated ionic conductivity of Al_x-LLZO as a function of x at 298 K. The experimental data was extracted from several sources,[18–29,31–41] and the simulated values were obtained considering the computed D_{Li} and applying the Nernst-Einstein relationship:

$$\sigma_{\mathrm{Li}} = c_{\mathrm{Li}}(z_{\mathrm{Li}}F)^2\frac{D_{\mathrm{Li}}}{RT}, \tag{6}$$

where c_{Li} is the charge carrier density for Li, z_{Li} is the Li ionic charge, F is Faraday's constant, R is gas constant, and T is temperature.

There is no consensus in the literature on the predominant phase of Al_x-LLZO for $0.10 \leq x \leq 0.20$ at room temperature. Indeed, Chen et al.[28] and El-Shinawi et al.[40] found c-Al_x-LLZO at $x = 0.10 - 0.12$ using XRD, while Hu et al.[35] reported a combination of c- and t-phases within this concentration range. Notably, Botros et al.[34] and Tsai et al.[33] determined that the cubic/tetragonal mixture is preserved up to $x = 0.20$, although most works only report the presence of c-Al_x-LLZO at this Al content.[24,28,35,41,57] Matsuda et al.[30] and Djenadic et al.,[42] found the coexistence of c- and t-phases up to $x = 0.11$ and $x =$

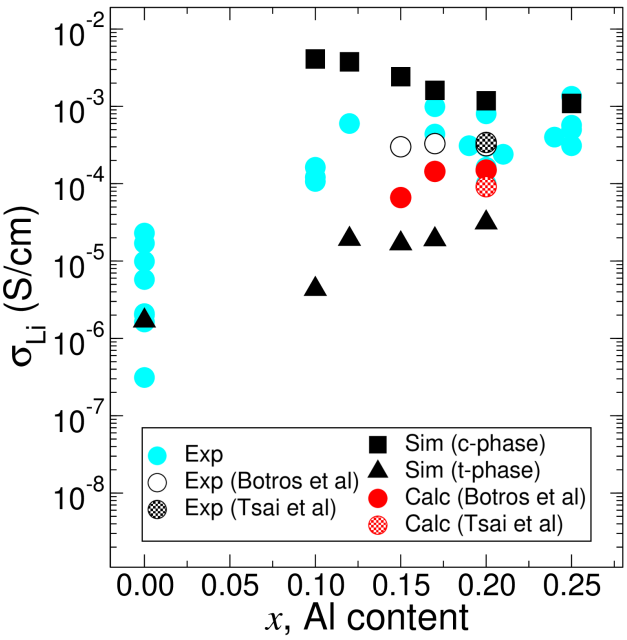

Figure 8: Experimental and simulated Li-ion conductivities, σ_{Li}, of Al_x-LLZO for $x = [0.0, 0.10, 0.12, 0.15, 0.17, 0.20, 0.25]$ at room temperature. Cyan circles correspond to experimental data taken from studies in Refs. 9,23–29,31,32,35–41,74. Empty and dotted circles correspond to the experimental conductivities from Botros et al.[33] and Tsai et al.,[33] respectively, who provide the percentages of c- and t-phases present in their samples. Filled squares (triangles) correspond to σ_{Li} for c-phase (t-phase) obtained in this work. Red filled and dotted circles correspond to the conductivities obtained by combining Bruggeman's model in Eq. 7 with the simulated σ_{Li} to represent the coexistence of t- and c-phases at the proportions reported by Botros et al.[33] and Tsai et al.,[33] respectively.

0.20, respectively. However, the conductivities obtained by these authors are 1-2 orders of magnitude below those reported by the majority sources. Given our inability to rationalize such results, we have not included them in Fig. 8. Nevertheless, the cell parameters extracted from XRD experiments of Matsuda et al. and Djenadic et al. are consistent with similar analyses from other authors.

The mentioned discrepancies can at least be partially explained by uncertainties in bulk Al content, as there is still no consensus on standardized synthesis protocols from where final samples are unaffected by experimental factors like sample preparation and synthesis conditions. For instance, if Al is deliberately added during synthesis using the sol-gel method, $LaAlO_3$ impurities are formed when the Al content in LLZO is high, and $La_2Zr_2O_7$ coexists with c-LLZO when the Li content is low.[25] Recent experiments employing microelectrodes for locally resolved impedance measurements revealed the existence of different conductivities in the bulk areas near the sample surface, which was attributed to compositional gradients at the interfaces.[75] Using a similar technique, Smetaczek et al.[76] found local gradients in conductivity and stoichiometry within the bulk region of Al_x-LLZO crystals. Surprisingly, these authors determined that no simple correlation exists between Li/Al content and ionic conduction. Indeed, high (low) levels of Li (Al) can correspond to either low or high conductivities. They concluded that compositional variations cannot alone explain the great variability in the conductivity data. One hypothesis put forward was that oxygen vacancies, first reported by Kubicek et al.,[77] could have a more significant impact on the conductivity than the scattering of the Li/Al content around the ideal stoichiometric value. In subsection 3.2.4 we explore an alternative or complementary mechanism: the co-existence of t- and c-LLZO.

Similarly, Wachter-Welzl et al.[41] observed that samples with identical Al contents ($x = 0.2$) prepared by a nominally identical solid state route and sintered at 1150°C and 1230°C could display significant variability in their conductivities, resulting from factors that cannot be explained by XRD measurements, such as gradients in the distribution of elements.

In this regard, the simulated data shown in Fig. 8 represents the maximum attainable ionic conductivity of ideally homogeneous and impurities-free Al_x-LLZO as a function of x in the c- (filled squares) and t- (filled triangles) phases. Clearly, the agreement between experimental and simulated data improves as x increases; the exception is $x = 0$, for which only the t-phase is stable at room temperature. At this composition, the simulated σ_{Li} (1.7×10^{-6} S/cm) is in reasonable agreement with the experimental values (3.1×10^{-7} - 1.7×10^{-5} S/cm). However, between $x = 0.1$ and 0.17 the simulated conductivities for c-phases (t-phases) overestimate (underestimate) the experimental results. For $x = 0.20$ and $x = 0.25$ the simulations of the c-phase nearly match the highest experimental conductivities. In the following, we compare in further detail the experimental and simulated data for each phase.

3.2.1 *c-phase:* There is a number of likely reasons why the simulations of c-Al_x-LLZO can predict satisfactorily the experimental data for $x \geq 0.20$. First, above $x = 0.20$ the c-phase is either the only one present or is largely predominant. Second, the impact of small uncertainties in the sample stoichiometry is less significant than at low values of x. Third, once the system has transitioned to the c-phase, its conductivity is likely less susceptible to relatively large stoichiometric uncertainties. The reason for this is atomistic in nature and comes from the slow variation of Li diffusivity in the c-phase for $x \geq 0.17$ discussed before: increasing the size of existing Al ion clusters reduces Li mobility in a slower manner than the formation of new clusters. Hence, the experimental conductivities at e.g. $x = 0.20$ and $x = 0.23$ are expectedly similar, mitigating the effect of relatively large uncertainties in the composition. Of course, even at high values of x the simulated structures will only be able to match, at best, the upper experimental conductivities, because the simulated systems are free of grain-boundaries, composition gradients, and other unavoidable synthesis defects.

3.2.2 *t-phase:* The general increase of σ_{Li} with x for the t-phase follows the trend established before (Subsection 3.1) for the diffusivity. Similar to the cubic garnet, simulation of t-Al_x-LLZO cannot reasonably predict the bulk of the experimental results for $0 < x \leq 0.17$.

Although the simulated conductivities increase with x, their values are always at least one order of magnitude below the experimental data compiled in Fig. 8 for $x > 0$. Since no universal agreement exists on the preferred configuration of Al_x-LLZO between $x = 0.10$ and $x = 0.20$, a more meaningful comparison between simulation and experiment in t-phase should be performed at $x < 0.10$. However, reliable data for such low Al contents is scarce, because accurate control of the sample stoichiometry is difficult and, from a practical standpoint, there is no technological interest in the low-conductive t-phase.

3.2.3 *Phase transition:* As mentioned above, the discrepancy between simulations of the c-phase and experiments at $x \leq 0.17$ is severe. Nonetheless, the trend displayed by our results is in agreement with observations from Travis et al.,[16] who used a combination of neutron diffraction and impedance spectroscopy to conclude that the conductivity of cubic Ta-substituted LLZO decreased monotonically with substituent content. This implies that the maximum in conductivity occurs exactly at the concentration of Al at which the phase transition occurs. This was suggested to be the case for Ga/Al-substituted LLZO,[53] although simulations over the entire range of concentrations, such as the ones performed here, were not done at the time, in order to verify this hypothesis.

3.2.4 *Phase coexistence:* While significant sources of variability exist and stoichiometric uncertainties lead to greater errors at small values of x, it is interesting to consider the possibility that the large over/under-estimations in the simulations are partly due to the coexistence of c- and t-Al_x-LLZO. Given the recently reported gradients in Al content within a single sample,[41] one potential scenario is that Al-rich regions crystallize in the c-phase, while the Al-poor regions form the t-phase. The second potential scenario is that thermodynamic equilibrium can be established between the two phases at the same x. To the best of our knowledge, neither scenario can be categorically neglected. Assuming that thermodynamic equilibrium exists between the c- and t-phases at some Al contents, we can estimate the proportion of each phase through an adequate mixing model. Here, we will assume that both phases mix randomly and homogeneously at the microscopic scale. Then, according to

Bruggeman's effective medium model,[78]

$$\nu_c \frac{\sigma_c - \sigma_m}{\sigma_c + 2\sigma_m} + \nu_t \frac{\sigma_t - \sigma_m}{\sigma_t + 2\sigma_m} = 0, \tag{7}$$

where ν_i is phase volume fraction, σ_i is conductivity and $i = \{c, t, m\}$ denotes the cubic, tetragonal, and mixed phases, respectively. By equating the c-phase volume fraction ν_c to the experimental values, it is possible to determine the theoretical conductivity of the mixed c- and t-phases using Eq. 7. Moreover, because the densities of the c- and t-phases are very similar, the volume fractions can be assumed equivalent to the mass fractions, ω_i (which are reported in the literature). Considering the experimental works by Botros et al.[34] and Tsai et al.,[33] who report mixed cubic/tetragonal samples with c-phase percentages ($100\omega_c$) of 26.4%, 34.5% and 34.0% for $x = 0.15,\ 0.17$ and 0.20, and 26% for $x = 0.20$, respectively, we estimated the corresponding mixed phase conductivities by using conductivities simulated over the range of Al content. The predictions are shown in Fig. 8 as red circles, while the measurements from Botros et al. and Tsai et al. are highlighted through the empty circles. Our predictions are in good agreement with the conductivities provided by Botros et al. and Tsai et al., reproducing the experimental results better than either of the pure phases at all Al contents (albeit only by a small margin at $x = 0.20$, where the estimated c-phase conductivity is nearly as accurate).

Certainly, further investigation is required to unequivocally determine whether cubic / tetragonal phase coexistence has more profound roots than a synthesis artifact, such as the difficulty of avoiding gradients in Al content. Even under those circumstances, if the mixing assumptions under which Eq. 7 are valid and the gradients in x are small, the methodology formulated here constitutes a sound alternative to estimate σ_m if the fraction of each phase is known. Alternatively, we put forward that when phase separation can be confirmed experimentally, the measurement of σ_m, together with our simulated conductivities, can be used to extract the percentage of each phase present in the sample using Eq. 7.

4. Conclusions

In this work, we use MD and the advanced atomistic simulation technique, GSHMC, to explore Li transport in Al-substituted LLZO at several Al contents in both tetragonal and cubic LLZO. Existing force fields were optimized in order to precisely reproduce reported cell parameters for both phases. The study is confined to room temperature conditions because of its practical relevance and abundance of experimental measurements; therefore, very long simulations (up to 200 ns, the longest reported for this material to the best of our knowledge) were required to correctly predict the diffusional regime in t-LLZO (D_{Li} 10^{-6}-10^{-5} m^2/s). Our simulations provide ideal upper and lower limits on the Li-ion conductivity for Al concentrations between 0 and 0.25 Al pfu, demonstrating a decrease (increase) in Li-ion conductivity with Al content in perfect c- (t-) phase. The difference in conductivity trends can be explained by considering that Al ions added to c-LLZO tend to trap their associated Li vacancies and neighboring Li ions. In contrast, analysis of the local environment of tetrahedrally coordinated Al ions in substituted t-LLZO reveals that Li ions are pushed to occupy previously inaccessible tetrahedral sites, which increases the number of possible diffusion paths.

There is no consensus in the literature on what the predominant phase of Al-substituted LLZO is for Al contents between 0.10 and 0.20 Al pfu. Indeed, while some authors only report the presence of the cubic structure within this concentration range, recent works also describe a combination of c- and t-phases. Given the likely existence of gradients in Al content within a single sample,[41] one potential explanation is that Al-rich crystallize in the c-phase, while those regions with lower Al content form in the t-phase. The second potential explanation is that thermodynamic equilibrium can be established between the two phases at some substituent concentrations. We show that the proposed simulation approach can be combined with an effective medium theory and the available experimental data to link the proportions of c- and t-phases present in a sample with the resulting conductivities. The predicted conductivities are indeed in good agreement with experimental measurements up

to 0.2 Al pfu, indicating that phase coexistence may be a common phenomenon. Overall, our study proposes an analytical approach to interpret Li-ion conductivity in Al_x-LLZO samples based on phase coexistence between cubic and tetragonal structures. Our theoretical findings provide new insight into the understanding of currently available experimental data and might help in the interpretation of future measurements, not only in the case of Al-substituted LLZO garnets, but also when using other substituent elements.

Acknowledgement

We acknowledge the financial support by the Ministerio de Economía y Competitividad (MINECO) of the Spanish Government through grants ENE2016-81020-R, MTM2016-76329-R (AEI/FEDER, EU) and BCAM Severo Ochoa accreditation SEV-2017-0718. This work was supported by the BERC 2018-2021 Program and by ELKARTEK Programme, grant KK-2018/00054, funded by the Basque Government. The SGI/IZO-SGIker UPV/EHU, the i2BASQUE academic network, and the Barcelona Supercomputer Center (QCM-2016-3-0002) are acknowledged for computational resources.

References

(1) Nitta, N.; Wu, F.; Lee, J. T.; Yushin, G. *Materials Today* **2015**, *18*, 252 – 264.

(2) Tarascon, J.-M.; Armand, M. *Nature* **2001**, *414*, 359.

(3) Takada, K. *Acta Materialia* **2013**, *61*, 759 – 770.

(4) Kato, Y.; Hori, S.; Saito, T.; Suzuki, K.; Hirayama, M.; Mitsui, A.; Yonemura, M.; Iba, H.; Kanno, R. *Nature Energy* **2016**, *1*, 16030.

(5) Bachman, J. C.; Muy, S.; Grimaud, A.; Chang, H.-H.; Pour, N.; Lux, S. F.; Paschos, O.;

458 Maglia, F.; Lupart, S.; Lamp, P.; Giordano, L.; Shao-Horn, Y. *Chemical Reviews* **2016**,
459 *116*, 140–162.

460 (6) Sun, C.; Liu, J.; Gong, Y.; Wilkinson, D. P.; Zhang, J. *Nano Energy* **2017**, *33*, 363 –
461 386.

462 (7) Murugan, R.; Thangadurai, V.; Weppner, W. *Angewandte Chemie International Edi-*
463 *tion* **2007**, *46*, 7778–7781.

464 (8) Thangadurai, V.; Pinzaru, D.; Narayanan, S.; Baral, A. K. *The Journal of Physical*
465 *Chemistry Letters* **2015**, *6*, 292–299.

466 (9) Thangadurai, V.; Narayanan, S.; Pinzaru, D. *Chemical Society Reviews* **2014**, *43*, 4714–
467 4727.

468 (10) Awaka, J.; Kijima, N.; Hayakawa, H.; Akimoto, J. *Journal of Solid State Chemistry*
469 *France* **2009**, *182*, 2046–2052.

470 (11) Adams, S.; Rao, R. P. *Journal of Materials Chemistry* **2012**, *22*, 1426–1434.

471 (12) Geiger, C. A.; Alekseev, E.; Lazic, B.; Fisch, M.; Armbruster, T.; Langner, R.;
472 Fechtelkord, M.; Kim, N.; Pettke, T.; Weppner, W. *Inorganic Chemistry* **2011**, *50*,
473 1089–1097.

474 (13) Deviannapoorani, C.; Dhivya, L.; Ramakumar, S.; Murugan, R. *Journal of Power*
475 *Sources* **2013**, *240*, 18 – 25.

476 (14) Li, Y.; Han, J.-T.; Wang, C.-A.; Xie, H.; Goodenough, J. B. *Journal of Materials*
477 *Chemistry* **2012**, *22*, 15357–15361.

478 (15) Ishiguro, K.; Nemori, H.; Sunahiro, S.; Nakata, Y.; Sudo, R.; Matsui, M.; Takeda, Y.;
479 Yamamoto, O.; Imanishi, N. *Journal of The Electrochemical Society* **2014**, *161*, A668–
480 A674.

(16) Travis, T.; Asma, S.; D., J. M.; Ashfia, H.; L., A. J.; Jeff, W.; Jeff, S. *Advanced Energy Materials* **2015**, *5*, 1500096.

(17) Ohta, S.; Kobayashi, T.; Asaoka, T. *Journal of Power Sources* **2011**, *196*, 3342 – 3345.

(18) Howard, M. A.; Clemens, O.; Kendrick, E.; Knight, K. S.; Apperley, D. C.; Anderson, P. A.; Slater, P. R. *Dalton Transactions* **2012**, *41*, 12048–12053.

(19) Shinawi, H. E.; Janek, J. *Journal of Power Sources* **2013**, *225*, 13 – 19.

(20) Bernuy-López, C.; Manalastas, W.; López del Amo, J. M.; Aguadero, A.; Aguesse, F.; Kilner, J. A. *Chemistry of Materials* **2014**, *26*, 3610–3617.

(21) Rettenwander, D.; Geiger, C. A.; Tribus, M.; Tropper, P.; Amthauer, G. *Inorganic Chemistry* **2014**, *53*, 6264–6269.

(22) Jalem, R.; Rushton, M.; Manalastas, W.; Nakayama, M.; Kasuga, T.; Kilner, J. A.; Grimes, R. W. *Chemistry of Materials* **2015**, *27*, 2821–2831.

(23) Kotobuki, M.; Kanamura, K.; Sato, Y.; Yoshida, T. *Journal of Power Sources* **2011**, *196*, 7750–7754.

(24) Li, Y.; Han, J.-T.; Wang, C.-A.; Vogel, S.; Xie, H.; Xu, M.; Goodenough, J. *Journal of Power Sources* **2012**, *209*, 278–281.

(25) Rangasamy, E.; Wolfenstine, J.; Sakamoto, J. *Solid State Ionics* **2012**, *206*, 28–32.

(26) Sudo, R.; Nakata, Y.; Ishiguro, K.; Matsui, M.; Hirano, A.; Takeda, Y.; Yamamoto, O.; Imanishi, N. *Solid State Ionics* **2014**, *262*, 151–154.

(27) Cheng, L.; Park, J.; Hou, H.; Zorba, V.; Chen, G.; Richardson, T.; Cabana, J.; Russo, R.; Doeff, M. *Journal of Materials Chemistry A* **2014**, *2*, 172–181.

(28) Chen, R.-J.; Huang, M.; Huang, W.-Z.; Shen, Y.; Lin, Y.-H.; Nan, C.-W. *Solid State Ionics* **2014**, *265*, 7–12.

(29) Zhang, Y.; Chen, F.; Tu, R.; Shen, Q.; Zhang, L. *Journal of Power Sources* **2014**, *268*, 960–964.

(30) Matsuda, Y.; Sakamoto, K.; Matsui, M.; Yamamoto, O.; Takeda, Y.; Imanishi, N. *Solid State Ionics* **2015**, *277*, 23–29.

(31) Suzuki, Y.; Kami, K.; Watanabe, K.; Watanabe, A.; Saito, N.; Ohnishi, T.; Takada, K.; Sudo, R.; Imanishi, N. *Solid State Ionics* **2015**, *278*, 172–176.

(32) David, I.; Thompson, T.; Wolfenstine, J.; Allen, J.; Sakamoto, J. *Journal of the American Ceramic Society* **2015**, *98*, 1209–1214.

(33) Tsai, C.-L.; Dashjav, E.; Hammer, E.-M.; Finsterbusch, M.; Tietz, F.; Uhlenbruck, S.; Buchkremer, H. *Journal of Electroceramics* **2015**, *35*, 25–32.

(34) Botros, M.; Djenadic, R.; Clemens, O.; Möller, M.; Hahn, H. *Journal of Power Sources* **2016**, *309*, 108–115.

(35) Hu, Z.; Liu, H.; Ruan, H.; Hu, R.; Su, Y.; Zhang, L. *Ceramics International* **2016**, *42*, 12156–12160.

(36) Rettenwander, D.; Redhammer, G.; Preishuber-Pflügl, F.; Cheng, L.; Miara, L.; Wagner, R.; Welzl, A.; Suard, E.; Doeff, M.; Wilkening, M.; Fleig, J.; Amthauer, G. *Chemistry of Materials* **2016**, *28*, 2384–2392.

(37) van den Broek, J.; Afyon, S.; Rupp, J. *Advanced Energy Materials* **2016**, *6*, 1600736.

(38) Zhang, Y.; Chen, F.; Tu, R.; Shen, Q.; Zhang, X.; Zhang, L. *Solid State Ionics* **2016**, *284*, 53–60.

(39) Kim, Y.; Jo, H.; Allen, J.; Choe, H.; Wolfenstine, J.; Sakamoto, J. *Journal of the American Ceramic Society* **2016**, *99*, 1367–1374.

(40) El-Shinawi, H.; Paterson, G. W.; MacLaren, D. A.; Cussen, E. J.; Corr, S. A. *Journal of Materials Chemistry A* **2017**, *5*, 319–329.

(41) Wachter-Welzl, A.; Kirowitz, J.; Wagner, R.; Smetaczek, S.; Brunauer, G.; Bonta, M.; Rettenwander, D.; Taibl, S.; Limbeck, A.; Amthauer, G.; Fleig, J. *Solid State Ionics* **2018**, *319*, 203–208.

(42) Djenadic, R.; Botros, M.; Benel, C.; Clemens, O.; Indris, S.; Choudhary, A.; Bergfeldt, T.; Hahn, H. *Solid State Ionics* **2014**, *263*, 49 – 56.

(43) Xu, M.; Park, M. S.; Lee, J. M.; Kim, T. Y.; Park, Y. S.; Ma, E. *Physical Review B* **2012**, *85*, 052301.

(44) Klenk, M.; Lai, W. *Physical Chemistry Chemical Physics* **2015**, *17*, 8758–8768.

(45) Burbano, M.; Carlier, D.; Boucher, F.; Morgan, B. J.; Salanne, M. *Physical Review Letters* **2016**, *116*, 135901.

(46) Chen, F.; Li, J.; Huang, Z.; Yang, Y.; Shen, Q.; Zhang, L. *The Journal of Physical Chemistry C* **2018**, *122*, 1963–1972.

(47) Rettenwander, D.; Blaha, P.; Laskowski, R.; Schwarz, K.; Bottke, P.; Wilkening, M.; Geiger, C. A.; Amthauer, G. *Chemistry of Materials* **2014**, *26*, 2617–2623.

(48) Akhmatskaya, E.; Reich, S. *Journal of Computational Physics* **2008**, *227*, 4934–4954.

(49) Escribano, B.; Lozano, A.; Radivojević, T.; Fernández-Pendás, M.; Carrasco, J.; Akhmatskaya, E. *Theoretical Chemistry Accounts* **2017**, *136*.

(50) Bonilla, M. R.; Lozano, A.; Escribano, B.; Carrasco, J.; Akhmatskaya, E. *The Journal of Physical Chemistry C* **2018**, *122*, 8065–8075.

(51) Klenk, M. J.; Lai, W. *Solid State Ionics* **2016**, *289*, 143 – 149.

(52) Pedone, A.; Malavasi, G.; Menziani, M. C.; Cormack, A. N.; Segre, U. *The Journal of Physical Chemistry B* **2006**, *110*, 11780–11795.

(53) García Daza, F. A.; Bonilla, M. R.; Llordés, A.; Carrasco, J.; Akhmatskaya, E. *ACS Applied Materials & Interfaces* **2019**, *11*, 753–765.

(54) Miara, L. J.; Richards, W. D.; Wang, Y. E.; Ceder, G. *Chemistry of Materials* **2015**, *27*, 4040–4047.

(55) Lander, L.; Reynaud, M.; Carrasco, J.; Katcho, N. A.; Bellin, C.; Polian, A.; Baptiste, B.; Rousse, G.; Tarascon, J.-M. *Physical Chemistry Chemical Physics* **2016**, *18*, 14509–14519.

(56) Buannic, L.; Orayech, B.; López Del Amo, J.-M.; Carrasco, J.; Katcho, N. A.; Aguesse, F.; Manalastas, W.; Zhang, W.; Kilner, J.; Llordés, A. *Chemistry of Materials* **2017**, *29*, 1769–1778.

(57) Rettenwander, D.; Redhammer, G.; Preishuber-Pflugl, F.; Cheng, L.; Miara, L.; Wagner, R.; Welzl, A.; Suard, E.; Doeff, M. M.; Wilkening, M.; Fleig, J.; Amthauer, G. *Chemistry of Materials* **2016**, *28*, 2384–2392.

(58) Escribano, B.; Akhmatskaya, E.; Mujika, J. *Central European Journal of Mathematics* **2013**, *11*, 787–799.

(59) Fernández-Pendás, M.; Akhmatskaya, E.; Sanz-Serna, J. *Journal of Computational Physics* **2016**, *327*, 434–449.

(60) Pronk, S.; Páll, S.; Schulz, R.; Larsson, P.; Bjelkmar, P.; Apostolov, R.; Shirts, M.; Smith, J.; Kasson, P.; Van Der Spoel, D.; Hess, B.; Lindahl, E. *Bioinformatics* **2013**, *29*, 845–854.

(61) Duane, S.; Kennedy, A.; Pendleton, B.; Roweth, D. *Physics Letters B* **1987**, *195*, 216–222.

(62) Akhmatskaya, E.; Fernández-Pendás, M.; Radivojević, T.; Sanz-Serna, J. *Langmuir* **2017**, *33*, 11530–11542.

(63) Horowitz, A. *Physics Letters B* **1991**, *268*, 247–252.

(64) Kennedy, A.; Pendleton, B. *Nuclear Physics B* **2001**, *607*, 456–510.

(65) Wee, C.; Sansom, M.; Reich, S.; Akhmatskaya, E. *Journal of Physical Chemistry B* **2008**, *112*, 5710–5717.

(66) Mujika, J.; Escribano, B.; Akhmatskaya, E.; Ugalde, J.; Lopez, X. *Biochemistry* **2012**, *51*, 7017–7027.

(67) Escribano, B.; Akhmatskaya, E.; Reich, S.; Azpiroz, J. *Journal of Computational Physics* **2015**, *280*, 1–20.

(68) Radivojević, T.; Fernández-Pendás, M.; Sanz-Serna, J.; Akhmatskaya, E. *Journal of Computational Physics* **2018**, *373*, 900–916.

(69) Kuhn, A.; Narayanan, S.; Spencer, L.; Goward, G.; Thangadurai, V.; Wilkening, M. *Physical Review B* **2011**, *83*, 094302.

(70) Andriyevsky, B.; Doll, K.; Jacob, T. *Materials Chemistry and Physics* **2017**, *185*, 210 – 217.

(71) Jalem, R.; Yamamoto, Y.; Shiiba, H.; Nakayama, M.; Munakata, H.; Kasuga, T.; Kanamura, K. *Chemistry of Materials* **2013**, *25*, 425–430.

(72) Reed, D. A.; Ehrlich, G. *Surface Science* **1981**, *105*, 603 – 628.

(73) Auerbach, S. M. *International Reviews in Physical Chemistry* **2000**, *19*, 155–198.

(74) Ramakumar, S.; Deviannapoorani, C.; Dhivya, L.; Shankar, L. S.; Murugan, R. *Progress in Materials Science* **2017**, *88*, 325 – 411.

(75) Wachter-Welzl, A.; Wagner, R.; Rettenwander, D.; Taibl, S.; Amthauer, G.; Fleig, J. *Journal of Electroceramics* **2017**, *38*, 176–181.

(76) Smetaczek, S.; Wachter-Welzl, A.; Wagner, R.; Rettenwander, D.; Amthauer, G.; Andrejs, L.; Taibl, S.; Limbeck, A.; Fleig, J. *J. Mater. Chem. A* **2019**, *7*, 6818–6831.

(77) Kubicek, M.; Wachter-Welzl, A.; Rettenwander, D.; Wagner, R.; Berendts, S.; Uecker, R.; Amthauer, G.; Hutter, H.; Fleig, J. *Chemistry of Materials* **2017**, *29*, 7189–7196.

(78) Landauer, R. *AIP Conference Proceedings* **1978**, *40*, 2–45.

Graphical TOC Entry

Some journals require a graphical entry for the Table of Contents. This should be laid out "print ready" so that the sizing of the text is correct.
Inside the `tocentry` environment, the font used is Helvetica 8 pt, as required by *Journal of the American Chemical Society*.
The surrounding frame is 9 cm by 3.5 cm, which is the maximum permitted for *Journal of the American Chemical Society* graphical table of content entries. The box will not resize if the content is too big: instead it will overflow the edge of the box.
This box and the associated title will always be printed on a separate page at the end of the document.